An edge pedestal investigation for high-confinement tokamak plasmas

Weston M. Stacey
Fusion Research Center, Georgia Institute of Technology, Atlanta, Georgia 30332

(Received 14 November 2001; accepted 23 January 2002)

A model for the edge pedestal in high-confinement mode tokamak plasmas is described. Separate gradient scale lengths of the density and of the ion and electron temperatures are calculated from transport and atomic physics considerations, and a common pedestal width is calculated from either a magnetohydrodynamic pedestal β-limit or from neutral penetration considerations. Predictions of the model for a representative gas fueled tokamak model problem are discussed vis-à-vis measured values of pedestal gradient scale lengths and widths, ballooning mode limits, and scaling with operational parameters. © *2002 American Institute of Physics.* [DOI: 10.1063/1.1461846]

I. INTRODUCTION

The steep gradient edge pedestal region in high confinement mode (*H*-mode) tokamak discharges apparently plays a major role in determining the overall plasma performance. For example, there is experimental evidence relating the edge gradients to the $L-H$ transition[1] and relating the value of the temperature at the top of the pedestal to the core thermal energy content.[2] Furthermore, the evolution of edge gradients has been postulated as a trigger mechanism for the $L-H$ (low to high mode) transition,[3,4] and strong edge gradients have been identified as important for the suppression of MARFEs[5] (multifaceted asymmetric radiation from edge). Accordingly, the physics of the edge pedestal is an area of active experimental and theoretical investigation (see Ref. 6 for a recent review).

The edge pedestal may be characterized by six characteristic lengths, the first three of which are the gradient scale lengths of density, electron temperature and ion temperature in the sharp gradient region $[L_n \equiv -n/(dn/dr),\ L_{T_e} \equiv -T_e/(dT_e/dr),\ L_{T_i} \equiv -T_i/(dT_i/dr)]$. The second three lengths are the distances into the plasma from the separatrix (the ''widths'') over which the respective sharp gradients extend $(\Delta_n, \Delta_{T_e}, \Delta_{T_i})$. While similar in magnitude, these different characteristic lengths are usually distinct.

A number of different proposals have been put forward for the physical mechanisms that determine these characteristic lengths. MHD (magnetohydrodynamic) ballooning mode instabilities have long been thought to impose a lower limit on the pressure gradient scale length, $L_p(L_n, L_{T_e}, L_{T_i})$, and thus on the combination of density and temperature gradient scale lengths. However, recent experimental results[2,7] in DIII-D indicate that the edge pressure gradient can exceed the nominal ideal stability limit for ballooning modes by a factor of 2 to 3. This observation is consistent with the theoretical prediction of access to a second stability regime through a gap between the ballooning and peeling mode stability boundaries[8–11] which removes the ballooning mode stability limit for high-*n* modes and allows a steeper pressure gradient. Another explanation for the observation of edge pressure gradients exceeding the nominal ideal ballooning limit is that ballooning modes are stabilized by diamagnetic effects.[12]

MHD pressure gradient constraints impose a lower limit on the pressure gradient scale length, $L_p(L_n, L_{T_e}, L_{T_i})$, but do not define the individual density and temperature gradient components. Transport constraints (i.e. the requirement that the density and temperature gradient scale lengths are consistent with the particle and convective heat fluxes flowing across the edge pedestal region), on the other hand, separately define the L_n, L_{T_e}, and L_{T_i}.[13] Since the onset of MARFEs usually is followed by an H–L transition and since there is a threshold upper limit on the temperature gradient scale lengths for MARFE onset,[5] the MARFE stability requirement imposes an upper limit on the temperature gradient scale lengths. We propose in this paper a model in which the gradient scale lengths L_n, L_{T_e}, and L_{T_i} are calculated from the transport constraints but are further constrained to satisfy a MHD ballooning or peeling mode lower limit constraint on the pressure gradient scale length and a MARFE upper limit constraint on the temperature gradient scale lengths.

There are a number of theories also for the width of the sharp-gradient region in the edge pedestal, most of them associated with either ion orbit loss[14,15] or shear suppression of turbulence.[16–20] The influx of neutral particles into the pedestal region plays a role in two of these theories.[16,18] In general, no distinction is made among the widths of the sharp gradient regions for the density and the ion and electron temperatures. We propose in this paper two models for a common width $(\Delta_n = \Delta_{T_e} = \Delta_{T_i} = \Delta_{\mathrm{TB}})$ of the edge pedestal, or ''transport barrier'' (TB). In the first model, we propose that there is a β-limit on the pedestal pressure that limits the extent (width) of the sharp gradient region in the edge of the plasma. In the second model, we propose that the width of the sharp gradient region is limited by the effective neutral penetration distance.

II. GRADIENT SCALE LENGTHS

A. Transport constraints, including atomic physics

The gradient scale lengths in the edge pedestal must be consistent with the nonradiative heat and particle fluxes from

the core across the edge pedestal region into the scrape-off layer, taking into account the modification of those fluxes by atomic physics effects. We repeat here, for completeness, the derivation of this transport constraint.[13]

The ion flux passing through the transport barrier is increased by the ionization of neutrals

$$\frac{d\Gamma_\perp}{dr} = n n_o \langle \sigma v \rangle_{\rm ion} \equiv n \nu_{\rm ion}, \tag{1}$$

where n_o is the neutral atom density and $\langle \sigma v \rangle_{\rm ion}$ is the specific ion–electron ionization rate averaged over the energy distributions of both species. Integrating this equation from the top of the pedestal (''ped'') outward to the separatrix (''sep'') yields

$$\Gamma_\perp^{\rm sep} - \Gamma_\perp^{\rm ped} = \int_{\Delta {\rm TB}} n \nu_{\rm ion} dr \equiv n_{TB} \nu_{\rm ion}^{\rm TB} \Delta_{\rm TB}, \tag{2}$$

where $\Gamma_\perp^{\rm sep}$ is the net outward ion current crossing the separatrix from the plasma edge into the scrape-off layer, $\Gamma_\perp^{\rm ped}$ is the net outward ion current from the core plasma into the sharp gradient region, or transport barrier, at the top of the pedestal, and $\Delta_{\rm TB}$ is the width of the region from the pedestal to the separatrix.

In order to define an average density gradient in the transport barrier, we define an average value of the net outward ion current

$$\Gamma_\perp^{\rm av} \equiv \tfrac{1}{2}(\Gamma_\perp^{\rm sep} + \Gamma_\perp^{\rm ped}), \tag{3}$$

that we then relate to the general form for the ion current

$$\Gamma_\perp^{\rm av} = -D \frac{dn}{dr} + n_{\rm TB} v_p = n_{\rm TB}(D L_n^{-1} + v_p), \tag{4}$$

where D is the diffusion coefficient and v_p is the pinch velocity. We may eliminate either $\Gamma_\perp^{\rm sep}$ or $\Gamma_\perp^{\rm ped}$ by using Eqs. (2) and (3) to obtain

$$L_n = \frac{D}{\Gamma_\perp^{\rm sep} \Big/ \left(n_{TB} - \frac{1}{2} v_{\rm ion}^{\rm TB} \Delta_{\rm TB} - v_p \right)} = \frac{D}{\Gamma_\perp^{\rm ped} \Big/ \left(n_{\rm TB} + \frac{1}{2} v_{\rm ion}^{\rm TB} \Delta_{\rm TB} - v_p \right)}. \tag{5}$$

The second form of Eq. (5) shows that the ionization of neutrals and any inward particle pinch ($v_p < 0$), as well as any reduction in diffusion coefficient, will decrease the density gradient scale length (steepen the gradient) in the transport barrier.

Assuming that the ions and electrons cross the transport barrier in a time short compared to the equilibration time, the net outward electron and ion nonradiative heat fluxes in the transport barrier are described by

$$\frac{dQ_{\perp e}}{dr} = -n n_0 \langle \sigma v \rangle_{\rm ion} E_{\rm ion} - n n_z L_z \equiv -n \nu_{\rm ion} E_{\rm ion} - n n_z L_z \tag{6}$$

and

$$\frac{dQ_{\perp i}}{dr} = -n n_0^c \langle \sigma v \rangle_{\rm at} \frac{3}{2} T \equiv -n \nu_{\rm at}^c \frac{3}{2} T_i, \tag{7}$$

where $E_{\rm ion}$ is the ionization energy, n_z and L_z are impurity density and radiation emissivity, n_0^c is the uncollided (cold) neutral density in the transport barrier, and $\langle \sigma v \rangle_{\rm at}$ is the specific elastic scattering plus charge exchange reaction rate of previously uncollided (in the transport barrier) neutrals. These nonradiative heat fluxes are reduced by atomic physics cooling in the transport barrier. Equations (6) and (7) may be integrated across the transport barrier to obtain

$$Q_{\perp e}^{\rm sep} - Q_{\perp e}^{\rm ped} = -\int_{\Delta_{\rm TB}} n \nu_{\rm ion} E_{\rm ion} dr - \int_{\Delta_{\rm TB}} n n_z L_z dr \equiv -n_{\rm TB} \nu_{\rm ion}^{\rm TB} E_{\rm ion} \Delta_{\rm TB} - n_{\rm TB} (n_z L_z)_{\rm TB} \Delta_{\rm TB} \tag{8}$$

and

$$Q_{\perp i}^{\rm sep} - Q_{\perp i}^{\rm ped} = -\int_{\Delta_{\rm TB}} n \nu_{\rm at}^c \frac{3}{2} T_i dr \equiv -n_{\rm TB} \nu_{\rm at}^{c\,\rm TB} \tfrac{3}{2} T_i^{\rm TB} \Delta_{\rm TB}. \tag{9}$$

Proceeding as above, and equating the average nonradiative heat flux to the standard form

$$Q_\perp^{av} = -\chi n \frac{dT}{dr} + \frac{5}{2} T \Gamma_\perp = \chi n T L_T^{-1} + \frac{5}{2} T \Gamma_\perp, \tag{10}$$

leads to expressions for average electron and ion temperature gradient scale lengths in the transport barrier

$$L_{T_e} = \frac{\chi_e^{\rm TB}}{\left[\left(\frac{Q_{\perp e}^{\rm sep}}{n_{\rm TB} T_e^{\rm TB}} - \frac{5}{2} \frac{\Gamma_\perp^{\rm sep}}{n_{\rm TB}} \right) + \frac{1}{2} \Delta_{\rm TB} \left(\frac{(n_z L_z)_{\rm TB}}{T_e^{\rm TB}} + \nu_{\rm ion}^{\rm TB} \left(\frac{E_{\rm ion}}{T_e^{\rm TB}} + \frac{5}{2} \right) \right) \right]} = \frac{\chi_e^{\rm TB}}{\left[\left(\frac{Q_{\perp e}^{\rm ped}}{n_{\rm TB} T_e^{\rm TB}} - \frac{5}{2} \frac{\Gamma_\perp^{\rm ped}}{n_{\rm TB}} \right) - \frac{1}{2} \Delta_{\rm TB} \left(\frac{(n_z L_z)_{\rm TB}}{T_e^{\rm TB}} + \nu_{\rm ion}^{\rm TB} \left(\frac{E_{\rm ion}}{T_e^{\rm TB}} + \frac{5}{2} \right) \right) \right]} \tag{11}$$

and

$$L_{T_i}\frac{\chi_i^{\mathrm{TB}}}{\left[\left(\frac{Q_{\perp i}^{\mathrm{sep}}}{n_{\mathrm{TB}}T_i^{\mathrm{TB}}}-\frac{5}{2}\frac{\Gamma_{\perp}^{\mathrm{sep}}}{n_{\mathrm{TB}}}\right)+\frac{1}{2}\Delta_{\mathrm{TB}}\left(\frac{3}{2}\nu_{\mathrm{at}}^{c,\mathrm{TB}}+\frac{5}{2}\nu_{\mathrm{ion}}^{\mathrm{TB}}\right)\right]}=\frac{\chi_i^{\mathrm{TB}}}{\left[\left(\frac{Q_{\perp i}^{\mathrm{ped}}}{n_{\mathrm{TB}}T_i^{\mathrm{TB}}}-\frac{5}{2}\frac{\Gamma_{\perp}^{\mathrm{ped}}}{n_{\mathrm{TB}}}\right)-\frac{1}{2}\Delta_{\mathrm{TB}}\left(\frac{3}{2}\nu_{\mathrm{at}}^{c,\mathrm{TB}}+\frac{5}{2}\nu_{\mathrm{ion}}^{\mathrm{TB}}\right)\right]}, \tag{12}$$

where the χ's are average thermal diffusivities for ions and electrons in the transport barrier.

As Eqs. (5), (11), and (12) make clear, the gradient scale lengths in the transport barrier depend on the particle and convective heat fluxes flowing through the transport barrier (which must be determined by the particle and heat balances on the core plasma), on the transport coefficients in the transport barrier, on the average density and temperatures in the transport barrier and on the atomic physics particle sources and heat sinks in the transport barrier. Thus, these gradient scale lengths can not be determined just on the basis of a local model for the pedestal, but must take into account also the core plasma balance and the fueling and recycling of neutrals in the edge transport barrier.

B. MHD ballooning and peeling mode pressure gradient constraints

The gradient scale lengths determined from transport considerations are constrained by MHD stability requirements on the maximum pressure gradient, or equivalently on the minimum pressure gradient scale length. This constraint is conventionally written in the form

$$-\left(\frac{dp}{dr}\right)_{\mathrm{crit}}=\frac{\alpha_c\left(\frac{B^2}{2\mu_0}\right)}{q_{95}^2R}, \tag{13}$$

where B is the toroidal field, R is the major radius, q_{95} is the safety factor at the 95% flux surface, and α_c is in general a function of magnetic shear and plasma geometry. The nominal ideal ballooning mode value of α_c is of order unity in the absence of second stability access, shear reduction by bootstrap currents, etc.

Access to second stability for high toroidal mode number (n) modes increases α_c to the point at which lower toroidal mode number modes, which do not have access to second stability, become unstable. The presence of steep pressure gradients in the plasma edge will drive a bootstrap current, which will reduce the shear, which in turn will reduce the maximum stable edge pressure gradient. These effects may be represented by writing

$$\left(-\frac{dp}{dr}\right)_{\mathrm{crit}}=\frac{B^2/2\mu_0}{q_{95}^2R}C_sA_s(s)\left[s_0-2\frac{j_{bs}}{\langle j\rangle}\right]\equiv\alpha_c(s)\frac{\left(\frac{B^2}{2\mu_0}\right)}{q_{95}^2R}, \tag{14}$$

where $\langle j\rangle=I/\pi a^2\kappa$ is the average current density over the entire plasma cross section (minor radius "a" and elongation κ) and j_{bs} is the bootstrap current density in the edge. C_s is a quantity of order unity depending on the shear in the magnetic field and $A_s(s)$ is intended to contain the physics of the s-α diagram for ballooning modes and peeling modes (e.g., Refs. 8–11). The general effect of this physics is to increase A_s above unity because of finite Larmor radius (FLR) stabilization of high-n ballooning modes,[11] stabilization of all ballooning modes by ion diamagnetic drift effects,[12] access to the second stable regime,[8–11] etc.

The requirement for stability against ballooning and peeling modes

$$\left(-\frac{dp}{dr}\right)\leqslant\left(-\frac{dp}{dr}\right)_{\mathrm{crit}}, \tag{15}$$

can be written as a MHD constraint on the allowable values of the gradient scale lengths

$$L_p^{-1}\equiv\left(L_n^{-1}+\frac{T_e}{T_e+T_i}L_{T_e}^{-1}+\frac{T_i}{T_e+T_i}L_{T_i}^{-1}\right)\leqslant L_{\mathrm{MHD}}^{-1}\equiv\frac{1}{p}\left(-\frac{dp}{dr}\right)_{\mathrm{crit}}. \tag{16}$$

A major next task in the development of an edge pedestal model is the parameterization of $A_s(s)$. In the meantime, we will determine the gradient scale lengths from the transport and atomic physics constraints of the previous section and monitor the value of a "ballooning index"

$$BI\equiv p_{\mathrm{TB}}L_p^{-1}\Big/\left[\left(\frac{B^2}{2\mu_0}\right)\Big/q_{95}^2R\right]=\alpha_c^{\mathrm{eff}}. \tag{17}$$

When BI$<$1, the gradient scale lengths satisfy the nominal ideal ballooning mode constraint. However, since $\alpha_c\approx 2$ to 3 is routinely found in DIII-D,[7,11] BI$>$1 does not necessarily indicate an unstable edge pedestal.

C. MARFE stability constraint

Edge instabilities such as edge-localized modes (ELMs) and multifaceted asymmetric radiation from the edge (MARFEs) also could impose constraints on the allowable values of the gradient scale lengths. In general, the edge plasma recovers from an ELM event without losing H-mode confinement, but a MARFE event leads to a $H-L$ transition. Thus, we will implicitly assume that any ELMs present are taken into account in the definition of averaged transport coefficients, and we include explicitly only the MARFE instability limit in the model for gradient scale lengths constraints.

It has been shown theoretically[21] and demonstrated by numerical simulation[22] that $k_\parallel = (m + nqB_\theta/B)/qR \approx 0$ two-dimensional edge-localized modes (m and n are poloidal and toroidal mode numbers, respectively, q is the safety factor, and B and B_θ are the total and poloidal magnetic fields, respectively) are the first to become unstable in MARFE formation, because of the stabilizing effect of parallel heat conduction for finite $k_\parallel$ modes. A linear analysis of the stability of a poloidally uniform plasma edge density and temperature distribution to $k_\parallel \approx 0$ edge-localized modes leads to a prediction[5] of the onset condition for MARFEs. The MARFE index (MI) is defined as the ratio of the actual experimental electron density in the plasma edge to the predicted limiting edge density for MARFE onset

$$MI \equiv \frac{n_{\rm exp}}{n_{\rm MARFE}} = n_{\rm exp}^2 \left[f_z \left\{ (\nu + 1 - C^{(2)}) \frac{L_z}{T} \frac{\partial L_z}{\partial T} \right\} + f_o \left\{ \frac{E_{\rm ion}}{T} \left(\nu \frac{T}{\langle \sigma v \rangle_{\rm ion}} \frac{\partial \langle \sigma v \rangle_{\rm ion}}{\partial T} \right) \right\} + f_o^{\rm cold} \left\{ \frac{3}{2} (\langle \sigma v \rangle_{\rm cx} + \langle \sigma v \rangle_{el}) \left(\nu - 1 - T \frac{\partial (\langle \sigma v \rangle_{\rm cx} + \langle \sigma v \rangle_{el})/\partial T}{(\langle \sigma v \rangle_{\rm cx} + \langle \sigma v \rangle_{el})} \right) \right\} \right] \div \left[\frac{f_{\rm cond} Q_\perp}{T} (\nu L_T^{-1} + (C^{(2)} - 1) L_n^{-1}) \right]. \quad (18)$$

$C^{(2)}$ is a quantity less than unity associated with thermal friction ν characterizes the temperature dependence of the radial heat conductivity ($\chi \sim T^\nu$), the $\langle \sigma v \rangle$ are the ionization (ion), elastic scattering (el) and charge-exchange (cx) reaction rates averaged over the electron or ion Maxwellian distributions in the edge plasma, f_z is the impurity concentration, f_o is the total neutral atom concentration, $f_o^{\rm cold}$ is the previously uncollided ''cold'' neutral concentration, and $f_{\rm cond}$ is the conductive fraction of the nonradiative heat flux crossing the separatrix. A poloidally averaged neutral concentration must be used to evaluate these atomic physics reaction rates.

III. PEDESTAL WIDTH

A. Model 1: MHD pedestal β-limit constraint on pedestal width

We propose that a MHD stability β-limit on the maximum pedestal pressure determines the pedestal pressure width, Δ_p. For example, stability of the edge pedestal against MHD ideal pressure-driven surface modes imposes a maximum allowable value on the pedestal pressure[12]

$$p_{\rm crit} = \frac{8}{3} \frac{B^2/2\mu_0}{q_{95}^2} \left(\frac{T_i}{2(T_i + T_e)} \right)^{1/3} \left(\frac{\rho_i}{R} \right)^{2/3}, \quad (19)$$

where ρ_i is the ion gyroradius.

For a given edge pressure gradient scale length, L_p, and a given pressure at the separatrix ($p_{\rm sep}$ determined by divertor physics), the β-limit on the maximum allowable pedestal pressure, $p_{\rm crit}$, results in the constraint

TABLE I. Parameters for a DIII-D gas fueled model problem.

Input parameter		
major radius, R(m)	1.76	
plasma radius, a(m)	0.60	
elongation, κ	1.76	
triangularity, δ	0.22	
magnetic field, B(T)	2.0	
current, I(MA)	1.5	
source, S(#/s)	5×10^{21}	
heating, $P_{\rm NBI}$(MW)	5.0	
pinch, v_p(m/s)	-5.0	
pedestal $\chi_i = \chi_e$ (m^2/s)	1.0	
pedestal D (m^2/s)	0.2	
$H_{\rm ITER89P}$	2.0	
divertor	USN	
Calculated parameter	*Pedestal Model 1*	*Pedestal Model 2*
midplane separatrix n (#/m^3)	0.183×10^{20}	0.183×10^{20}
pedestal n (#/m^3)	0.408×10^{20}	0.369×10^{20}
line average n (#/m^3)	0.641×10^{20}	0.664×10^{20}
midplane separatrix T[a] (eV)	114	114
pedestal T[a] (eV)	212	277
core average T[a] (eV)	1830	1770
$\Delta_{\rm TB}$ (cm)	1.6	2.7
L_n (cm)	2.0	3.9
L_{T_e} (cm)	1.7	1.9
L_{T_i} (cm)	3.5	4.3

[a] $\frac{1}{2}(T_e + T_i)$.

$$p_{\rm crit} = n^{\rm ped}(T_i^{\rm ped} + T_e^{\rm ped}) = n_{\rm sep} e^{\Delta_p/L_n} (T_i^{\rm sep} e^{\Delta_p/L_{T_i}} + T_e^{\rm sep} e^{\Delta_p/L_{T_e}}), \quad (20a)$$

when $p_{\rm crit}$ is understood to pertain to the pressure at the top of pedestal, and in the constraint

$$p_{\rm crit} = n^{\rm TB}(T_i^{\rm TB} + T_e^{\rm TB}), \quad (20b)$$

when $p_{\rm crit}$ is understood to pertain to the average pressure over the pedestal region.

We set $\Delta_p = \Delta_n = \Delta_{T_i} = \Delta_{T_e} = \Delta_{\rm TB}$, set $p_{\rm TB} = (p_{\rm ped} + p_{\rm sep})/2 = p_{\rm crit}$ and solve $L_p^{-1} = -(dp/dr)/p$ to obtain

$$\Delta_{\rm TB} = L_p(\Delta_{\rm TB}) \ln \left(2 \frac{p_{\rm crit}}{p_{\rm sep}} - 1 \right) \equiv L_p(\Delta_{\rm TB}) G, \quad (21)$$

where the constraint of Eq. (20b) has been used. This ''common pedestal width'' approximation is made, at this stage of development of a pedestal model, for analytical convenience. We indicate later how a model with different pedestal widths can be developed. Using Eqs. (5), (11), (12), and (19) in Eq. (21) results in a quadratic equation in $\Delta_{\rm TB}$, which has the solution

$$\Delta_{\rm TB} = \frac{b}{2a} \left[\sqrt{1 + \frac{4aG}{b^2}} - 1 \right] \approx \frac{G}{b} \left[1 - \left(\frac{aG}{b^2} \right) + \left(\frac{aG}{b^2} \right)^2 - \cdots \right]. \quad (22)$$

The second form of this result is valid when atomic physics effects are not dominant; i.e., when $|aG/b^2| < 1$. The constants in Eq. (22) are

$$a \equiv \frac{1}{2}\left[-\frac{\nu_{\rm ion}}{D} + \gamma_i \frac{\left(\frac{3}{2}\nu_{\rm at}^c + \frac{5}{2}\nu_{\rm ion}\right)}{\chi_i} + \gamma_e \frac{\left(\frac{n_z L_z}{T_e} + \nu_{\rm ion}\left\{\frac{E_{\rm ion}}{T_e} + \frac{5}{2}\right\}\right)}{\chi_e}\right], \tag{23a}$$

$$b \equiv \left[\frac{(\Gamma_\perp^{\rm sep}/n - v_p)}{D} + \gamma_i \frac{\left(\frac{Q_{\perp t}^{\rm sep}}{nT_i} - \frac{5}{2}\frac{\Gamma_\perp^{\rm sep}}{n}\right)}{\chi_i} + \gamma_e \left(\frac{\left(\frac{Q_{\perp e}^{\rm sep}}{nT_e} - \frac{5}{2}\frac{\Gamma_\perp^{\rm sep}}{n}\right)}{\chi_e} \right) \right], \tag{23b}$$

and

$$\gamma_i \equiv \frac{T_i}{T_e + T_i}, \quad \gamma_e \equiv \frac{T_e}{T_e + T_i}. \tag{23c}$$

When atomic physics effects are not dominant, the leading order term for the pedestal width

$$\Delta_{\rm TB}^{(0)} \equiv \frac{G}{b} = \frac{\ln\left[\frac{16}{3}\frac{1}{2}\left(\frac{4\pi}{5\times 10^6 \mu_0}\right)^2 \left(\frac{B_\theta^2/2\mu_0}{p_{\rm sep}}\right)\frac{(1+\kappa^2)}{\varepsilon^2 g^2}\left(\frac{1}{2}\gamma_i\right)^{1/3}\left(\frac{\rho_i}{R}\right)^{2/3} - 1\right]}{\left[\left(\frac{\Gamma_\perp^{\rm sep}/n - v_p}{D}\right) + \gamma_i\left(\frac{\left(\frac{Q_{\perp i}^{\rm sep}}{nT_i} - \frac{5}{2}\frac{\Gamma_\perp^{\rm sep}}{n}\right)}{\chi_i}\right) + \gamma_e\left(\frac{\left(\frac{Q_{\perp e}^{\rm sep}}{nT_e} - \frac{5}{2}\frac{\Gamma_\perp^{\rm sep}}{n}\right)}{\chi_e}\right)\right]}, \tag{24}$$

is determined by the MHD pressure constraint and the edge transport physics. In this case, the atomic physics effects enter to higher order through the term (aG/b^2) in Eq. (22). The quantity $g \equiv [1+\kappa^2(1+2\delta^2-1.2\delta^3)][1.17-0.65\epsilon]/[1-\varepsilon^2]^2$ is a geometric factor arising from the definition $q_{95} = (5/2)(a^2/R)(B/I)g$.

B. Model 2: Neutral penetration constraint on pedestal width

The buildup in plasma density from the separatrix inward to the top of the density pedestal is due, at least in part, to the ionization of recycling and fueling neutrals that are diffusing inward across the separatrix, which implies that the limit of penetration of these neutrals into the plasma will play an important role in determining the extent of the steep density gradient region, or the density pedestal width, Δ_n. Using a simple diffusion theory model[23]

$$-\frac{d}{dr}\left(\frac{1}{3n\sigma_{\rm tr}}\frac{d\phi}{dr}\right) + n\sigma_{\rm ion} = 0, \tag{25}$$

for inward neutral atom transport and replacing the varying plasma density in the pedestal with an average value, $n_{\rm TB}$, it can be shown[24] that the neutral atom flux ($\phi = n_0 v_0$) attenuates exponentially into the plasma with an effective mean free path $\lambda_0 = [n_{\rm TB}(3\sigma_{\rm tr}\sigma_{\rm ion})^{1/2}]^{-1}$, i.e., that

$$\phi(r) = \phi(r=0)\exp(-r/\lambda_o), \tag{26}$$

where r is measured inward from the separatrix, $\sigma_{\rm ion}$ is the ionization cross section, $\sigma_{\rm tr} = \sigma_{\rm ion} + \sigma_{\rm cx}(1-\mu_{\rm cx}) + \sigma_{\rm el}(1-\mu_{\rm el})$ is the "transport" cross section, $\sigma_{\rm cx}$ and $\sigma_{\rm el}$ are the charge-exchange and elastic scattering cross sections, and $\mu_{\rm cx}$ and $\mu_{\rm el}$ are the average cosine of the neutral atom "scattering" angle in charge-exchange and elastic scattering collisions with plasma ions. Since the direction of the neutral atom emerging from a charge-exchange collision with a

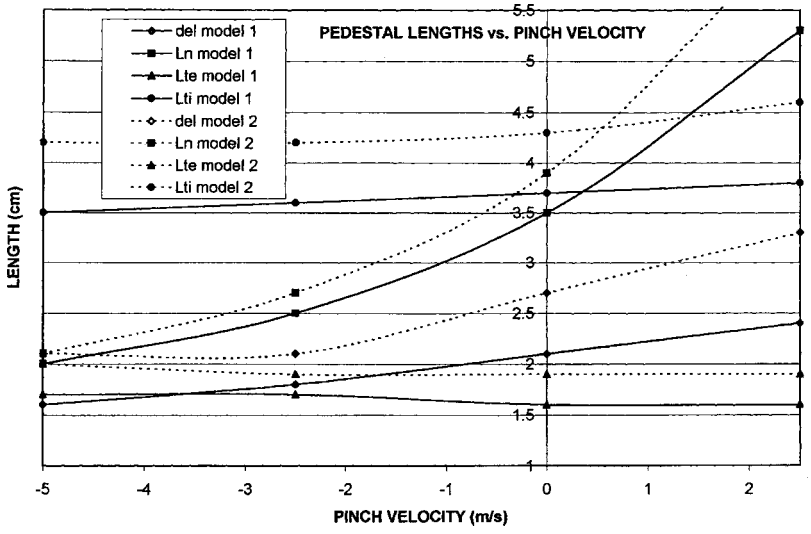

FIG. 1. Scaling of pedestal lengths with particle pinch velocity in a gas fueled DIII-D model problem ($R = 1.76$ m, $a = 0.60$ m, $\kappa = 1.76$, $\delta = 0.22$, $B = 2.0$ T, $I = 1.5$ MA, $P_{\rm nbi} = 5$ MW, $S = 5\times 10^{21}$ #/s, $\chi_e = \chi_i = 1.0$ m/s, $D = \chi_i/5$).

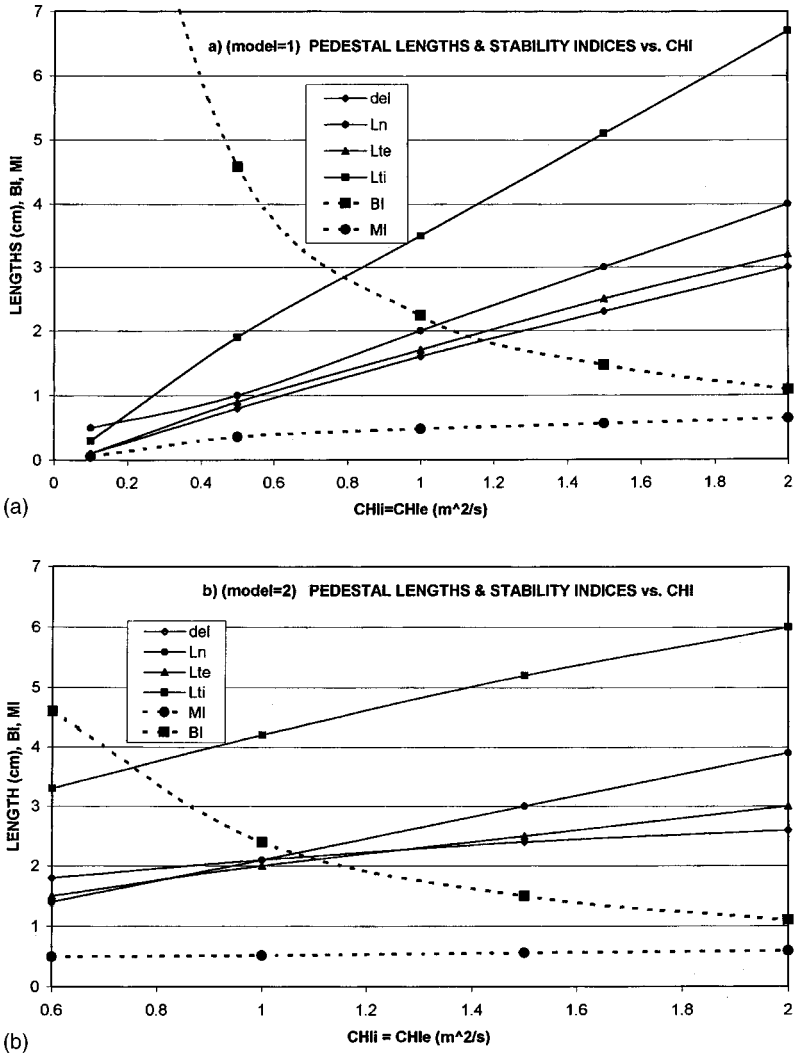

FIG. 2. Scaling of pedestal lengths with $\chi_e=\chi_i$ in a gas fueled DIII-D model problem ($R=1.76$ m, $a=0.60$ m, $\kappa=1.76$, $\delta=0.22$, $B=2.0$ T, $I=1.5$ MA, $P_{\mathrm{nbi}}=5$ MW, $S=5\times10^{21}$ #/s, $v_p=-5.0$ m/s, $D=\chi_i/5$) [(a) pedestal model 1; (b) pedestal model 2].

plasma ion is equally likely to be in any direction, $\mu_{\mathrm{cx}}=0$. For the elastic scattering of a neutral atom from an ion, $\mu_{\mathrm{el}}\approx 2/3A$, where A = ion mass/neutral mass.

A plausible approximation for the density width of the pedestal is the mean-free-path for neutral particle attenuation

$$\Delta_n=\lambda_0=[n_{\mathrm{TB}}(3\sigma_{\mathrm{tr}}\sigma_{\mathrm{ion}})^{1/2}]^{-1}. \tag{27}$$

We set $\Delta_{\mathrm{TB}}=\Delta_{T_i}=\Delta_{T_e}=\Delta_n$ in this model.

IV. MODEL PROBLEM CALCULATIONS

We now discuss a series of model problem calculations that were made to investigate the predicted magnitudes and parameter scalings of the pedestal models described above. The pedestal models have been incorporated in a code[25] that calculates particle and nonradiative heat fluxes through the pedestal, the plasma properties at the separatrix and at the divertor plate, the transport of recycling and gas-puffed neutrals into the pedestal and core, and the ballooning and peeling mode and the MARFE stability indices. This code was developed for the analysis of continuous gas fueled shots in DIII-D and has, to some extent, been benchmarked by such applications.[26,27] The model problem parameters are representative of DIII-D shots with gas fueling. We have used our familiarity with experimental results from such shots to generally guide the analysis, but have deferred the analysis of specific experimental results to a future paper.

The results labeled ''model 1'' refer to the use of the transport and atomic physics model of Sec. II to calculate gradient scale lengths and to the use of the pedestal β-limit model of Sec. III A to calculate the pedestal width, while the results labeled ''model 2'' differ by the use of the neutral penetration model of Sec. III B to calculate the pedestal width. In both cases, the pedestal calculation is iterated to consistency with the core and divertor plasma calculations and with the neutral particle transport calculations, so that the mutual interactions among these calculations are consistently treated.

Three overarching conclusions of the calculations presented in this section are that the calculated pedestal gradient scale lengths and width are of the size measured experimentally in gas fueled DIII-D shots, that the calculated factor of about 2 for the ratio of ion to electron temperature gradient scale lengths is in agreement with the data for such shots, and that there is very little difference between the predictions of the β-limit and neutral penetration pedestal width models. The last two conclusions are suggested by the comparison of results from the two models for one set of model problem

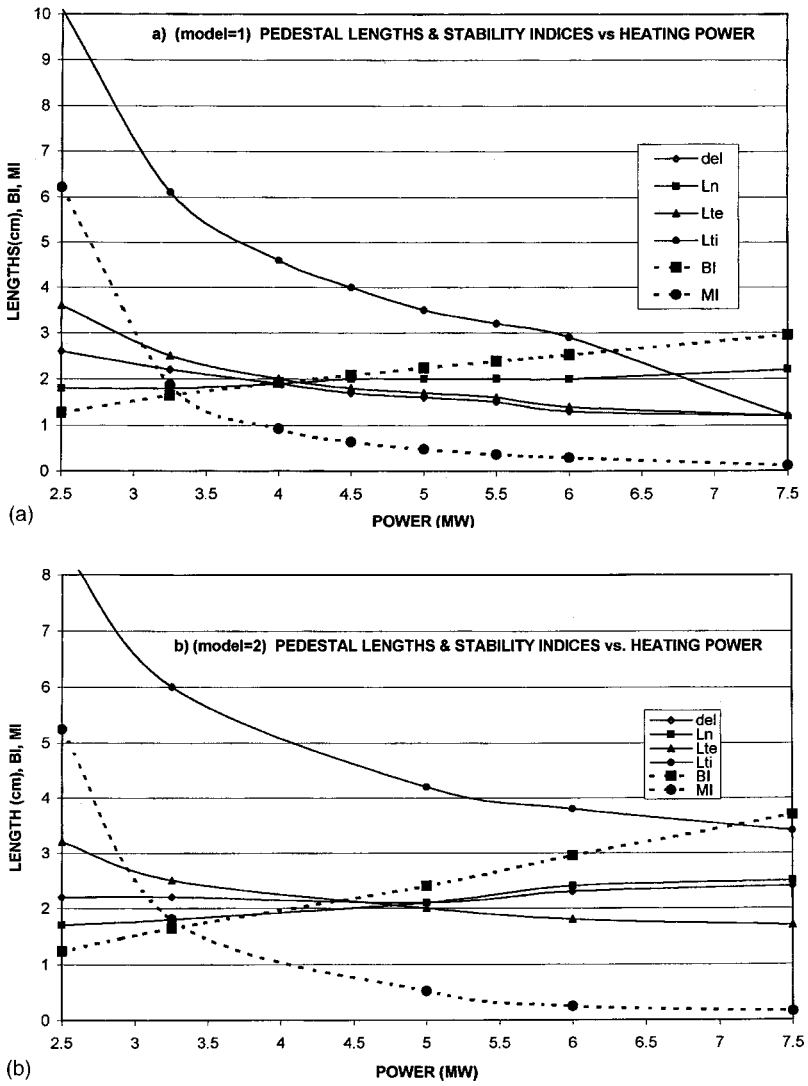

FIG. 3. Scaling of pedestal lengths with auxiliary heating power in a gas fueled DIII-D model problem ($R=1.76$ m, $a=0.60$ m, $\kappa=1.76$, $\delta=0.22$, $B=2.0$ T, $I=1.5$ MA, $S=5\times10^{21}$ #/s, $\chi_e=\chi_i=1.0$ m/s, $D=\chi_i/5$, $v_p=-5.0$ m/s) [(a) pedestal model 1; (b) pedestal model 2].

parameters shown in Table I and will become more apparent from the following discussion of the calculated parameter dependence of the two models.

A. Pinch velocity

The pedestal gradient scale lengths and width were calculated as a function of pinch velocity, and the results are shown in Fig. 1 (negative v_p corresponds to an inward particle pinch). The two models yield similar results, except for a small difference in magnitude. The different widths predicted by Eqs. (22) and (27) produce directly differences in the gradient scale lengths when used in Eqs. (5), (11), and (12). In addition, the different widths predicted by Eqs. (22) and (27) cause differences in pedestal densities, temperatures, and particle and heat fluxes, which indirectly produce further differences in the widths and gradient scale lengths. The density gradient scale length of Eq. (5) is quite sensitive, the pedestal width is somewhat less sensitive, and the temperature gradient scale lengths are relatively insensitive to v_p.

An inward particle pinch is usually needed to match experimental results in transport simulations of DIII-D shots.[28] In the gas fueled DIII-D shots that we have examined, the density and electron temperature gradient scale lengths were similar, and the ion temperature gradient scale length was significantly larger, which argues for the use of v_p less than about -3 m/s. We adopted $v_p=-5$ m/s for the remaining investigations.

B. Pedestal transport coefficients

The pedestal gradient scale lengths and width were calculated as a function of pedestal transport coefficients $\chi_e=\chi_i=5$D, and the results are shown in Fig. 2. The two models predict a similar increase of all pedestal lengths with increasing transport coefficients. Density and electron temperature gradient scale lengths and pedestal widths in the range of about 1–4 cm, and larger values of the ion temperature gradient scale length, are common in the gas fueled DIII-D discharges with which we are familiar.

The ballooning and peeling mode stability index (BI) and the MARFE index (MI) are also plotted in Fig. 2. The edge pressure gradients in this type of DIII-D discharge typically exceed the nominal ideal ballooning mode limit by a factor of 2 to 3, but the stability of cases with values of BI >3 is questionable. This would seem to indicate that pedes-

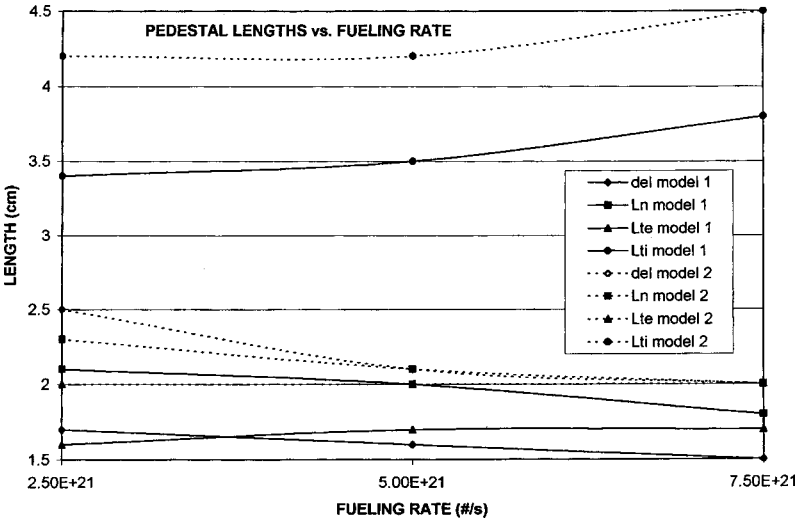

FIG. 4. Scaling of pedestal lengths with fueling rate in a gas fueled DIII-D model problem ($R=1.76$ m, $a=0.60$ m, $\kappa=1.76$, $\delta=0.22$, $B=2.0$ T, $I=1.5$ MA, $P_{\mathrm{nbi}}=5$ MW, $\chi_e=\chi_i=1.0$ m/s, $D=\chi_i/5$, $v_p=-5.0$ m/s).

tal transport coefficients less than $\chi_{e,i}\approx 0.8-0.9\ \mathrm{m}^2/\mathrm{s}$ are inconsistent with gradient scale lengths on the order of a few cm. These calculations are stable against MARFE onset (MI$<$1) for all values of the pedestal transport coefficients considered.

C. Heating power

A series of calculations was performed to evaluate the effect of auxiliary heating power on the calculated pedestal gradient scale lengths and width, and the results are presented in Fig. 3. Both models predict that temperature gradient scale lengths decrease with increasing heating power, particular the ion temperature gradient scale length, and that the density gradient scale length increases slightly with increasing heating power. Model 1 predicts a slight decrease in pedestal width with increasing heating power, while model 2 predicts a slight increase, but the difference is not significant.

The ballooning and peeling mode stability index (BI) increases with increasing heating power because of the decreasing gradient scale lengths, and the MARFE index (MI) decreases with heating power for the same reason. The highest power cases in Fig. 3 may be unstable to ballooning or peeling modes (BI$>$3), and the lowest power cases are surely unstable to the onset of MARFEs (MI$\gg$1).

D. Gas fueling rate

A series of calculations have been made with different gas fueling rates, and the resulting pedestal gradient scale lengths and widths are shown in Fig. 4. The temperature gradient scale lengths increase slightly, and the density gradient scale length and width decrease slightly with increasing fueling rate, in both models.

E. Magnetic field

The pedestal gradient scale lengths and width were calculated as a function of toroidal magnetic field, and the results are shown in Fig. 5. The temperature gradient scale lengths decrease slightly with increasing B for model 1, but increase significantly with increasing B for model 2. The density gradient scale length increases somewhat with increasing B for model 1, but is insensitive to B for model 2. The pedestal width decreases significantly with increasing B for model 1, but decreases only slightly for model 2.

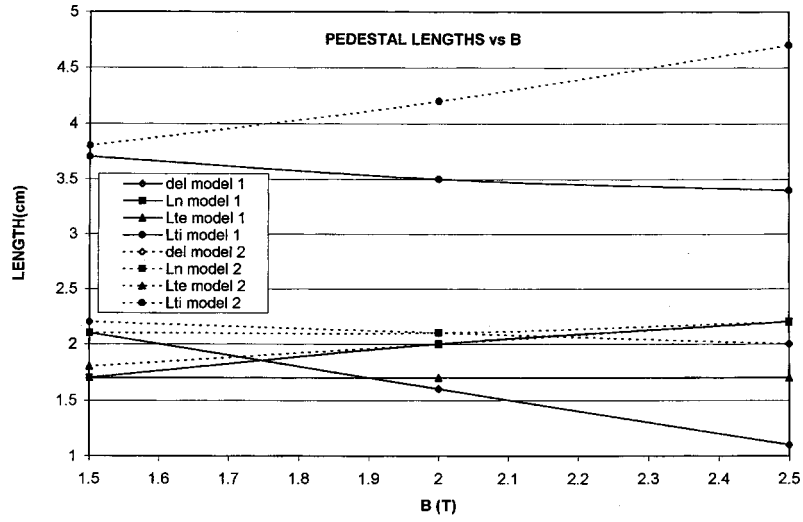

FIG. 5. Sensitivity of pedestal lengths to magnetic field in a gas fueled DIII-D model problem ($R=1.76$ m, $a=0.60$ m, $\kappa=1.76$, $\delta=0.22$, $I=1.5$ MA, $P_{\mathrm{nbi}}=5$ MW, $S=5\times10^{21}$ #/s, $\chi_e=\chi_i=1.0$ m/s, $D=\chi_i/5$, $v_p=-5.0$ m/s).

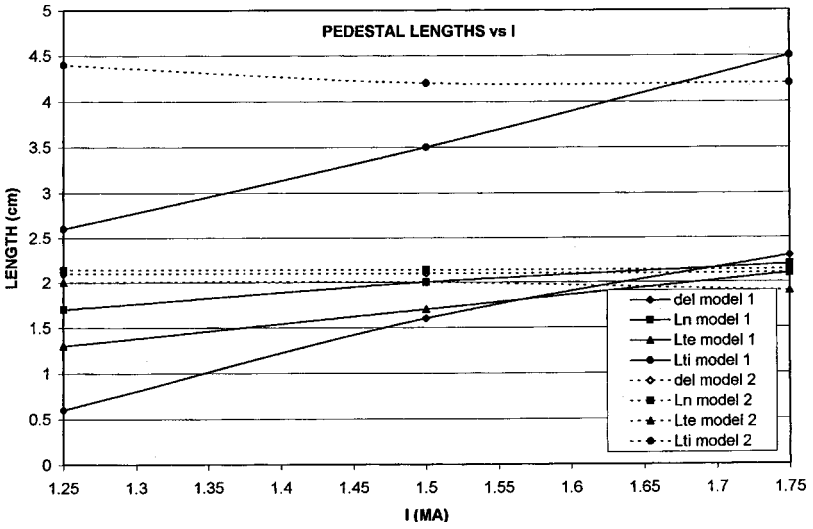

FIG. 6. Sensitivity of pedestal lengths to plasma current in a gas fueled DIII-D model problem ($R=1.76$ m, $a=0.60$ m, $\kappa=1.76$, $\delta=0.22$, $B=2.0$ T, $P_{\mathrm{nbi}}=5$ MW, $S=5\times10^{21}$ m/s, $\chi_e=\chi_i=1.0$ #/s, $D=\chi_i/5$, $v_p=-5.0$ m/s).

F. Plasma current

A series of calculations of pedestal gradient scale lengths and width as a function of plasma current was performed, and the results are shown in Fig. 6. The gradient scale lengths and pedestal width increase with I for model 1 but are insensitive to I for model 2.

V. SUMMARY AND CONCLUSIONS

We have proposed a model for calculating the density and ion and electron temperature gradient scale lengths in the edge pedestal based on requiring satisfaction of the respective transport equations. In this model, the gradient scale lengths in the edge pedestal depend on the particle and convective heat fluxes flowing through the transport barrier (which must be determined by the particle and heat balances on the core plasma), on the transport coefficients in the edge pedestal, on the average density and temperatures in the edge pedestal and on the atomic physics particle sources and heat sinks in the edge pedestal. Thus, these gradient scale lengths cannot be determined just on the basis of a local calculation for the pedestal, but must be calculated taking into account also the core plasma balance and the fueling and recycling of neutrals in the edge pedestal. We have also proposed additional constraints on the gradient scale lengths prescribed by the requirements for stability of MHD ballooning and peeling modes and on stability of MARFEs, which will impose lower and upper, respectively, limits on allowable values for the gradient scale lengths in the edge pedestal. We have also proposed two models for calculating the width of the edge pedestal, one based on a pedestal β-limit and the other based on neutral particle penetration.

Model problem calculations representative of DIII-D gas fueled discharges have been performed to investigate the predictions of these pedestal models. The principal conclusions of these calculations are: (1) that the calculated pedestal gradient scale lengths and width are of the size measured experimentally in such shots; (2) that the calculated factor of about 2 for the ratio of ion to electron temperature gradient scale lengths is in agreement with the data for such shots; and (3) that there is little difference between the predictions of the β-limit and neutral penetration pedestal width models. Because of the dependence of the pedestal model calculation on coupled core and divertor plasma and fueling and recycling neutral transport calculations, a comparison of the predictions of the model with experimental scaling results for pedestal parameters that are in the literature would require a substantial modeling effort, which is beyond the scope of this paper. Instead, we calculated predicted scaling relations for a DIII-D model problem. We plan a detailed comparison over a range of DIII-D shots in the future.

We note that the model presented in this paper does not explicitly address two experimentally observed features of the edge pedestal—the dependence of pedestal parameters on plasma shape[2,29] and the existence of different widths of the steep gradient regions for density and ion and electron temperatures. The present model has some implicit shape dependence through the effect of elongation and triangularity on the surface area used in calculating the nonradiative heat and particle fluxes, q_{95}, connection length along the field line from the midplane to the divertor plate, etc., but whether this is sufficient to account for the observed shape dependence remains to be tested. In principle, extension of the model to calculate different widths of the sharp gradient regions for the density and the ion and electron temperatures by adding two additional constraint equations to the set of four equations that are presently solved for the three gradient scale lengths and the common width is straightforward, but we elect to further investigate the predictions of the present model against experimental data first.

[1]R. J. Groebner, D. M. Thomas, and R. D. Deranian, Phys. Plasmas **8**, 272 (2001).
[2]T. H. Osborne, J. R. Ferron, R. J. Groebner *et al.*, Plasma Phys. Controlled Fusion **42**, A175 (2000).
[3]K. H. Burrell, Phys. Plasmas **4**, 1499 (1997).
[4]P. W. Terry, Rev. Mod. Phys. **72**, 109 (2000).
[5]W. M. Stacey, Plasma Phys. Controlled Fusion **39**, 1245 (1997); Fusion Technol. **36**, 38 (1999).
[6]A. E. Hubbard, Plasma Phys. Controlled Fusion **42**, A15 (2000).
[7]R. J. Groebner and T. H. Osborne, Phys. Plasmas **5**, 1800 (1998).
[8]R. L. Miller, Y. R. Lin-Liu, T. H. Osborne, and T. S. Taylor, Plasma Phys. Controlled Fusion **40**, 753 (1998).

[9]J. W. Connor, R. J. Hastie, H. R. Wilson, and R. L. Miller, Phys. Plasmas **5**, 2687 (1998).
[10]H. R. Wilson and R. L. Miller, Phys. Plasmas **6**, 873 (1999).
[11]J. R. Ferron, M. S. Chu, G. L. Jackson *et al.*, Phys. Plasmas **7**, 1976 (2000).
[12]B. N. Rogers and J. F. Drake, Phys. Plasmas **6**, 2797 (1999).
[13]W. M. Stacey, Phys. Plasmas **8**, 4073 (2001).
[14]K. C. Shaing, Phys. Fluids B **4**, 290 (1992).
[15]V. V. Parail, H. Y. Guo, and J. Lingertat, Nucl. Fusion **39**, 369 (1999).
[16]F. L. Hinton and G. M. Staebler, Phys. Fluids B **5**, 1281 (1993).
[17]P. H. Diamond, V. B. Lebedev, D. E. Newman, and B. A. Carreras, Phys. Plasmas **2**, 3685 (1995).
[18]P. H. Diamond, *Proceedings, 26th EPS Conference on Controlled Fusion Plasma Physics*, Maastricht, 1998 (EPS, Geneva, 1999), Vol 23J, p. 1466.
[19]M. Sugihara, *Proceedings, 26th EPS Conference on Controlled Fusion Plasma Physics*, Maastricht, 1998 (EPS, Geneva, 1999), Vol 23J, p. 1449.
[20]H. R. Wilson and J. W. Connor, *Proceedings, 24th EPS Conference on Controlled Fusion Plasma Physics Berchtesgaden*, 1996 (EPS, Geneva, 1997), Vol 21A, p. 289.
[21]W. M. Stacey, Phys. Plasmas **3**, 2673 (1996).
[22]A. Deploey, R. Van der Linden *et al.*, Plasma Phys. Controlled Fusion **39**, 423 (1997).
[23]W. M. Stacey, E. W. Thomas and T. M. Evans, Phys. Plasmas **2**, 3740 (1995).
[24]W. M. Stacey, *Nuclear Reactor Physics* (Wiley-Interscience, New York, 2001), p. 50.
[25]W. M. Stacey, Phys. Plasmas **8**, 3673 (2001).
[26]W. M. Stacey, M. A. Mahdavi, R. Maingi, and T. W. Petrie, Phys. Plasmas **6**, 3941 (1999).
[27]W. M. Stacey and T. W. Petrie, Phys. Plasmas **7**, 4931 (2000).
[28]J. Mandrekas, Georgia Tech, personal communication (2000).
[29]W. Suttrop, O. Gruber, B. Kurzan *et al.*, Plasma Phys. Controlled Fusion **42**, A97 (2000).